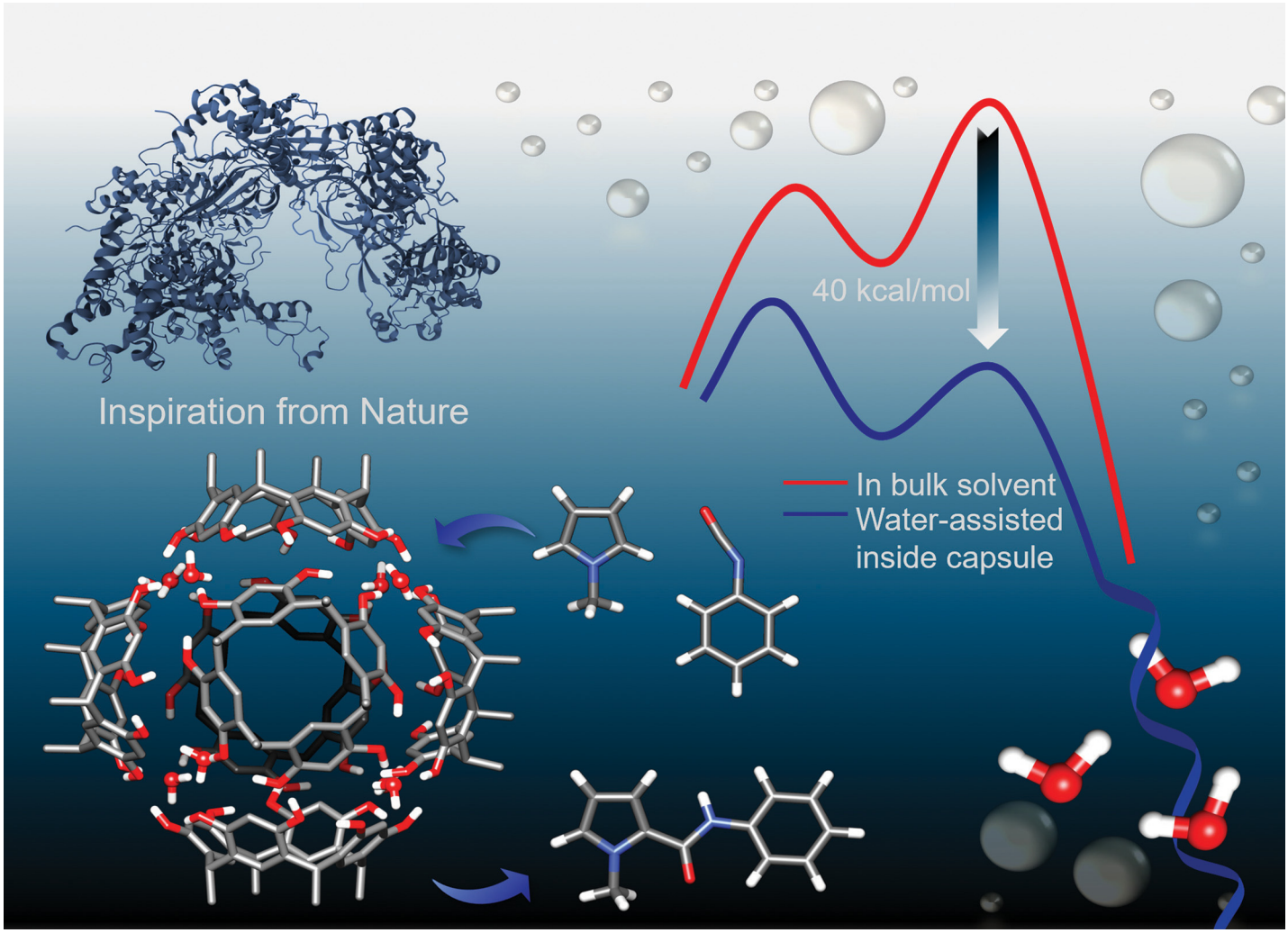

Showcasing research from the laboratory of Dr Lisa Roy, Computational Catalysis Group, Indian Institute of Technology Kharagpur, India

Unveiling the role of water in the coupling of pyrroles and isocyanates to amidopyrroles inside a hexameric resorcinarene capsule

This cover image showcases the crucial role of non-structural water molecules trapped inside the cavity of a self-assembled hexameric-resorcinarene capsule that facilitates the reaction of N-methylpyrrole and phenyl isocyanate to generate amidopyrrole, significantly reducing the energy barrier as compared to the bulk solvent and demonstrating high-efficiency of organic transformations in locally water-enriched media, as pervasive and regulated as in nature.

Image reproduced by permission of Lisa Roy from *Phys. Chem. Chem. Phys.*, 2026, **28**, 9193.

As featured in:

See Lisa Roy *et al.*, *Phys. Chem. Chem. Phys.*, 2026, **28**, 9193.

PCCP

ROYAL SOCIETY OF CHEMISTRY

PAPER

View Article Online
View Journal | View Issue

Cite this: *Phys. Chem. Chem. Phys.*, 2026, **28**, 9193

Unveiling the role of water in the coupling of pyrroles and isocyanates to amidopyrroles inside a hexameric resorcinarene capsule

Sanat Kumar Mahapatra, [a] Bijoy Ghosh [b] and Lisa Roy *[b]

Received 6th May 2025,
Accepted 9th February 2026

DOI: 10.1039/d5cp01713k

rsc.li/pccp

DFT calculations uncovered the crucial role of non-structural water molecules trapped inside the cavity of a self-assembled hexameric resorcinarene capsule in the reaction between *N*-methylpyrrole and phenyl isocyanate to generate an amidopyrrole through two crucial steps: C–C coupling and a 1,3C → N proton wire mechanism. Incidentally, the reaction in the bulk solvent is energetically demanding and underscores the role of encapsulation. In fact, non-structural incorporation of water molecules modulates the acidity of the hexameric resorcinarene capsule through hydrogen-bonded networks. This results in a shift in the rate-determining transition state to the initial C–C coupling step inside the capsule, as opposed to the energy intensive proton-wire mechanism in solution. Thus, the incorporated water molecules within the supramolecular cavity helps in accelerating the overall rate of the acid-catalyzed transformation. Our work, thus, indicates the advantage of the ubiquitous presence of water-enriched local domains in providing utmost control to the supramolecule in the catalytic process. These local hydrophilic domains with water clusters, encapsulated within organic molecules, emulate the kinetics, selectivity and mass transfer observed in some natural processes. The enhanced catalytic activity is primarily attributed to water molecule's ability to stabilize the reactants, products, intermediates or transition states through remote bond polarization, or proton shuttling, or ability of water to act as a co-catalyst.

Introduction

Supramolecular self-assembled capsules and cages are fascinating chemical discoveries that allow well-defined control over the stereo- and regio-selective outcomes of the chemical processes occurring inside their host cavities.[1] These simple yet architecturally complex assemblies possess unique shapes and rigid frameworks to host diverse substrates of various sizes, with specific recognition of guest molecules, in a solvent-free microenvironment. Interestingly, the trapped molecules display modified chemical properties compared with those in the bulk solvent due to the pre-organization of substrates to a specific conformation within the supramolecular cavities, which leads to the desired chemical conversions.[2] Notably, chemical transformations within the confined chambers of supramolecules draw inspiration from the active site of enzymes (Scheme 1),[2b] where the substrates are surrounded by the enzymatic pocket and the reactions are controlled by the collective effort of the optimum fitting of the substrate and non-covalent interactions exerted by the secondary coordination spheres,[3] resulting in catalytic activity under mild conditions. Similarly, supramolecular capsules and cages accommodate guest molecules in a locally electrostatic and dispersion-dominated chemical environment,[4] suppressing undesired alternative transformations in bulk solvent. Hence, these supramolecular catalysts offer atom-economic reactions and hold excellent promise as highly sustainable bio-mimicking materials for achieving accelerated reaction kinetics.[5] However, a major limitation in reducing the gap between enzyme catalysis and biomimicking supramolecular catalysis for large-scale organic synthesis lies in the understanding of the principles for substrate activation in nanoconfined environments, where both steric effects and attractive van der Waals interactions are expected to intervene. The major challenge stems from the arduous identification and isolation of reactive intermediates during the reaction of host–guest complexes, by kinetic or dynamic NMR measurements, which are precluded by complex self-assembly and reversible encapsulation thermodynamics on the timescales of seconds[6a] or minutes.[6b] Hence, understanding the key mechanistic aspects would offer enzyme-like precise reactivity controls and the possibility of designing systems that can achieve high-throughput synthesis of value-added chemicals.

Recently, several supramolecular research groups have unfolded key reactions utilizing the self-assembled hexameric

[a] *Institute of Chemical Technology Mumbai – IOC Odisha Campus Bhubaneswar, Bhubaneswar 751013, India*
[b] *Department of Education, Indian Institute of Technology Kharagpur, Kharagpur 721302, India. E-mail: L.Roy@edu.iitkgp.ac.in*

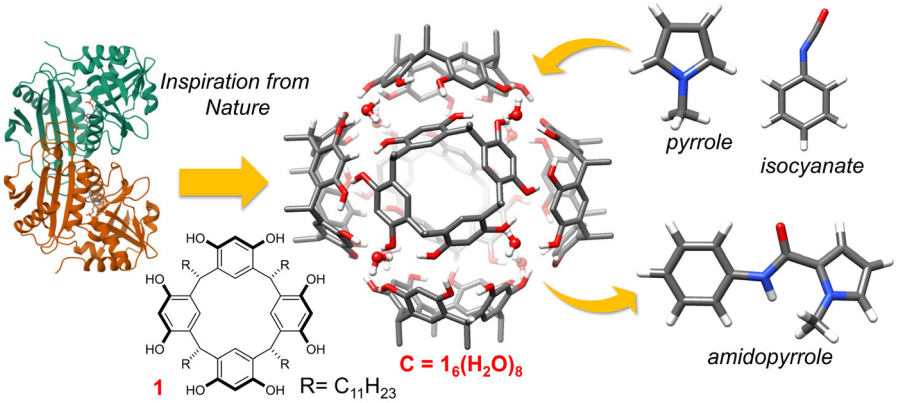

Scheme 1 Amidopyrrole formation from pyrrole and isocyanate in the hexameric resorcinarene capsule.[7b]

resorcinarene capsule **C** (Scheme 1).[7] Particularly interesting is the coupling of pyrroles and isocyanates to yield amidopyrroles in water-saturated chloroform in the mandatory presence of the capsule (Scheme 2), as reported by La Manna and co-workers in a recent study.[7b] This is extremely relevant in the context of druggable targets and inhibitory activities by molecular cage systems.[8] Originally reported by Atwood and MacGillivray,[9] capsule **C** in its solid state consists of a chiral spherical molecular assembly of six resorcinarene molecules and eight water molecules, held together by 60 hydrogen bonds. In an apolar solvent medium, the capsule features a well-defined cavity with an internal volume of about 1375 Å^3 and elevated Brønsted acidity (pK_a = 5.6 as referenced by protonation of pyridine)[7d] compared with the monomeric units due to the optimal existence of the H-bond network. Furthermore, a combined NMR spectroscopy and classical molecular dynamics (MD) simulation study identified two distinct conformers of the hexameric undecyl-resorcin[4]arene capsule ($\mathbf{C_A}$ and $\mathbf{C_B}$), featuring 8 and 15 hydrogen-bonded water molecules.[10,11] In fact, peripheral structural changes in the capsule effectuated by water molecules are believed to modulate the acidity of the supramolecular assembly, resulting in a 10-fold enhancement in the catalytic rate of an acid-catalysed Diels–Alder reaction by $\mathbf{C_B}$ as compared to $\mathbf{C_A}$.[10] Additionally, NMR diffusion studies detected several chloroform molecules inside the cavity of this superstructure, further adding layers of complexity to the self-assembly strategy.[12] Indeed, the capsule is surmised to have a strong affinity towards zwitterionic tetrahexylammonium bromide over chloroform molecules, indicating a strongly electrostatic host environment.[12] Hence, during self-assembly in H_2O-saturated chloroform (Scheme 2), one cannot rule out the trapping of activated non-structural water molecules in addition to the structural water molecules in the H-bonded networks. This concept is in line with the discovery of isolated water droplets inside a $Ga^4L_6^{12-}$ supramolecular tetrahedral cage employing THz absorption spectroscopy and *ab initio* molecular dynamics.[13] Although mechanistic studies on cavity-controlled selectivity are reported in the literature,[4,10,14] to date, an understanding of the role of trapped water molecules in reactivity is underexplored and warrants a thorough investigation. This, we believe, will open new channels to achieve highly efficient organic transformations in locally water-enriched media, as pervasive and regulated in Nature.

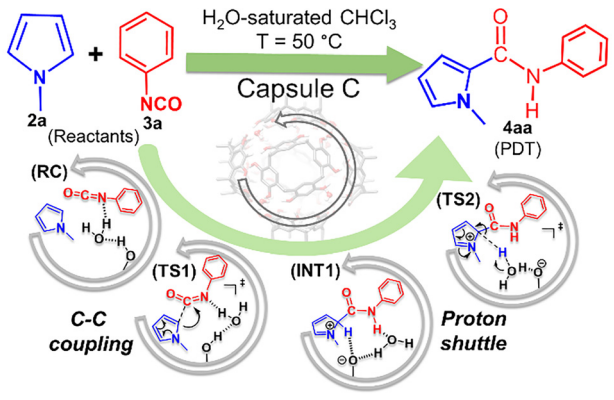

Scheme 2 Reaction conditions for the coupling of **2a** and **3a** to yield **4aa** in the presence of the capsule **C**, with snapshots of the proposed reaction species.

In the present work, therefore, we undertake a DFT study to explore the binding of additional non-structural water molecules, which have greater geometrical flexibility than the water molecules in the hydrogen-bonded networks of capsule **C**, and unravel the mechanistic intricacies of the coupling between *N*-methylpyrrole (**2a**) and phenyl isocyanate (**3a**) (Scheme 2). We hypothesize two crucial steps: C–C bond formation through nucleophilic attack of the pyrrole on the carbonyl of the isocyanate and a 1,3C → N proton wire mechanism through acid–base catalysis (Scheme 2).

Computational details

Density functional theory calculations were performed within the Gaussian 09 and ORCA 5.0.3 suites of quantum chemical packages.[15] To compensate for the high computational cost, the bulky undecyl alkyl group of the capsule (the so-called "feet") was replaced with methyl substituents. Modelling the formation of amidopyrrole inside the capsule with an

additional water molecule results in a system containing a total of 486 atoms. Geometry optimizations and identification of relevant stationary states of such a large system with DFT are impractical. Hence, an *in silico* investigation was conducted using Morokuma and co-workers' ONIOM method,[16] which builds upon the subtractive or extrapolative QM/MM formalism such that the total energy is given by eqn (1).

$$E_{\mathrm{ONIOM(QM/MM)}} = E_{\mathrm{QM,model}} + E_{\mathrm{MM,real}} - E_{\mathrm{MM,model}}, \quad (1)$$

i.e. the total energy of the whole (''real'') system is evaluated as the QM energy of the model system ($E_{\mathrm{QM,model}}$), in addition to the MM energy of the real system ($E_{\mathrm{MM,real}}$), minus the MM energy of the model system ($E_{\mathrm{MM,model}}$). In our approach, during geometry optimizations, the substrates **2a** and **3a**, together with one monomer of the cavitand, strongly interacting through H-bonds and the additional water molecule, comprising 102 atoms, were treated with DFT(M06-2X/6-31G(d,p)) and the rest of the supramolecular assembly by the semi-empirical PM6 method. This is a standard practice in some of the recent literature.[7a,c] Notably, in most of the earlier mechanistic studies with DFT, only two units of the host molecules were envisioned to form a capsule.[4,14] Since conventional DFT calculations scale cubically ($O(N^3)$), the computational cost for $\sim$500 atoms is enormous; thus, relatively cheaper alternatives are required for geometry optimizations and vibrational analysis. Hence, we utilized a two-layer ONIOM2 (QM1:QM2) method for optimizations of large systems with the M06-2X/6-31G(d,p)//PM6 level of theory (see Fig. S4), where the target energy of the real system, $E_{\mathrm{high,real}}$, is given by[16]

$$E_{\mathrm{high,real}} \approx E_{\mathrm{ONIOM2(high:low)}} = E_{\mathrm{high,model}} + E_{\mathrm{low,real}} - E_{\mathrm{low,model}}. \quad (2)$$

An *S*-value test was conducted to diagnose the accuracy of the low-level method (PM6) to describe the electronic effect or the ''substituent effect'' of the large ''real'' system (Table S5) as compared to the high-level method (M062X/6-31G(d,p)).[16] A ΔS-value of $\sim$0 suggested that the low-level method PM6 can be appropriately used in combination with the present high-level method, M06-2X/6-31(d,p) (Table S5). Conformational searches were performed manually by evaluating several conformers of the minimum and maximum structures, and the lowest energy geometries are reported. However, in the absence of the capsule, *i.e.* in implicit solvent (**S**) and assisted by a resorcin-arene monomer (**M**), the optimizations were computed at the M06-2X/6-31G(d,p) level. The structures were always optimized in implicit solvent by employing the polarizable continuum model (CPCM) with chloroform (ε = 4.71) as the solvent. Harmonic vibrational frequencies were computed at the same level of theory to distinguish transition states (with one negative Hessian index) from minima (with all positive Hessian indices). The non-thermal zero-point energy (ZPE) correction and the thermal corrections to enthalpy and Gibbs free energy were obtained from frequency calculations, using standard approximations at 298.15 K and 1 atm. pressure. Moreover, the electronic energies were refined by single-point calculations with full QM(DFT) calculations over all atoms (including 486 atoms for the reactions inside capsule) in the solvent phase with the B3LYP functional,[17] overlaid with Grimme's empirical dispersion (D3BJ) term,[18] employing the IOP (3/124 = 40) keyword, in conjugation with the larger triple-ξ Def2-TZVP basis set on all atoms. To mimic the mixed solvent of water and chloroform at 1 : 1 ratio within the domain of the CPCM solvation model, the following dielectric parameters of water were used: static dielectric constant (ε = 78.35), dynamic dielectric constant (ε_∞ = 1.77), hydrogen-bond acidity (1.17) and basicity (0.4), the surface tension of the solvent at interface (23.23), carbon aromaticity (0.0) and electronegative halogenicity (0.0), while the following parameters of chloroform were considered: static dielectric constant (ε = 4.7), dynamic dielectric constant (ε_∞ = 2.09), hydrogen-bond acidity (0.15) and basicity (0.02), the surface tension of the solvent at interface (38.39), carbon aromaticity (0.0) and electronegative halogenicity (0.75), following Paton and co-workers' methodology.[19] Relative Gibbs free energies are evaluated by adding thermal corrections obtained from vibrational analyses to the solvent-phase electronic energies. Additionally, a correction term of 1.89 kcal mol^{-1} (at 298.15 K) was included as necessary to account for the standard-state concentration of 1 M, especially to account for the solvation of many species, including micro-solvated water molecules, taking part in the transition state.[20] Thus, the discussions in the main text are provided based on Gibbs free energies (kcal mol^{-1}) at the B3LYP-D3(BJ)/CPCM {H_2O : $CHCl_3$ = 1 : 1}/Def2-TZVP//ONIOM[M06-2X/CPCM($CHCl_3$)/6-31G(d,p):PM6] level of theory. Furthermore, to evaluate the dependence on the DFT functional, energies are computed at B3LYP/CPCM {H_2O : $CHCl_3$ = 1 : 1}/Def2-TZVP//ONIOM[M06-2X/CPCM($CHCl_3$)/6-31G(d,p):PM6] and M06-2X/CPCM {H_2O : $CHCl_3$ = 1 : 1}/Def2-TZVP//ONIOM[M06-2X/CPCM($CHCl_3$)/6-31G(d,p):PM6] (see Table S2). To check for dependence on solvent dielectric constant, single-point energies are also conducted in chloroform as solvent with B3LYP-D3(BJ), M06-2X and B3LYP functionals (see Table S3).

To verify the dependence of the low-level method on predicting the structures and thereby affecting the overall relative energies, we have conducted additional geometry optimizations at ONIOM[B3LYP-D3(BJ)/ALPB($CHCl_3$)/Def2-SVP:XTB] with ORCA 5.0.3[15b] and further single-point energy refinements at the B3LYP-D3(BJ)/ALPB($CHCl_3$)/Def2-TZVP level of theory. For all geometry optimizations, the following thresholds were used: convergence tolerance of 5×10^{-6} E_h for energy changes, 3×10^{-4} E_h per Bohr for maximum gradients, 1×10^{-4} E_h per Bohr for root-mean-square (RMS) gradients, 4×10^{-3} Bohr for maximum displacements, and 2×10^{-3} Bohr for RMS displacements. The numerical integration Grid6 was used throughout. Tight convergence criteria with an energy tolerance of 1×10^{-8} E_h for self-consistent field (SCF) achievement were utilized for all ORCA computations.

To gather an in-depth analysis of the key interactions responsible for relative energies, local energy decomposition (LED) partitioning of DLPNO-CCSD(T)/def2-TZVPP was utilized.[21] The theoretical background of this useful tool has

been detailed elsewhere.[21] In principle, the binding energy (ΔE) between a pair of fragments X and Y is hypothesized to consist of "geometric preparation energy" ($\Delta E_{\text{geo-prep}}$) or the amount of strain required to distort them from their equilibrium structures to an optimal point of interaction and the inter-fragment interaction energy (ΔE_{int}). The latter is further decomposed into various physical components, such as electrostatic interaction (ΔE_{elstat}), quantum mechanical exchange ($\Delta E_{\text{exchange}}$), charge-transfer correlation (ΔE_{CT}), and the London dispersion energy (ΔE_{disp}). In short, ΔE_{int} is summed up into dispersive (ΔE_{disp}) and non-dispersive ($\Delta E_{\text{non-disp}}$) components. Hence, according to this scheme, the relative free energy of activation for a transition state is given by:

$$\begin{aligned}\Delta G^{\ddagger} &= \Delta G^{\ddagger}_{\text{corr}} + \Delta E^{\ddagger} = \Delta G^{\ddagger}_{\text{corr}} + \Delta E^{\ddagger}_{\text{geo-prep}} + \Delta E^{\ddagger}_{\text{int}} \\ &= \Delta G^{\ddagger}_{\text{corr}} + \Delta E^{\ddagger}_{\text{geo-prep}} + \Delta E^{\ddagger}_{\text{disp}} \\ &\quad + \Delta E^{\ddagger}_{\text{no-disp}} \end{aligned} \tag{3}$$

where $\Delta G^{\ddagger}_{\text{corr}}$ incorporates solvent, thermal, and entropy corrections to Gibbs free energy.

NBO second-order perturbation theory analysis and Wiberg bond indices were calculated at the B3LYP-D3(BJ)/6-311+G(d,p) level, taking only the fragments of the substrates out of the relevant optimized geometries (Fig. S2). Within the context of conceptual DFT, Parr *et al.* defined the global electrophilicity index ω as:

$$\omega = \frac{\mu^2}{2\eta}, \tag{4}$$

where μ is the electronic chemical potential, and η is the chemical hardness.[22a] Furthermore, the electrophilic character of a local reactive site by a local electrophilicity index $\omega^{+}(r)$ is given by:

$$\omega^{+}(r) = \omega f^{+}(r), \tag{5}$$

where $f^{+}(r)$ is the Fukui function for nucleophilic attack obtained by using atomic populations. Similarly, nucleophilicity or electron-donating power ω^{-} is obtained from the formalism of Gazquez *et al.*,[22b] such that:

$$\omega^{-} = \frac{I^2}{2(I-A)}, \tag{6}$$

where I and A are the vertical ionization energy and electron affinity, respectively.

Results and discussion

We first pursued the reaction in the absence of the capsule to evaluate the role of encapsulation. As shown in Fig. 1, we hypothesize the formation of pre-reaction complexes, starting from separated molecules. Hence, separated reactants, water molecules or a single resorcin arene monomer are considered as the reference point for the free-energy profiles in Fig. 1 to properly address the entropic penalty. Next, C–C bond formation between the pyrrole and isocyanate substrates in the solvent medium takes place through **TS1@S$_U$** at a calculated energy barrier of 22.5 kcal mol^{-1}. Once the C–C coupled intermediate, **INT1@S$_U$**, is formed in a highly endergonic manner (ΔG = 22.1 kcal mol^{-1}), a 1,3C → N proton transfer takes place *via* **TS2@S$_U$** at a predominantly high barrier of 45.5 kcal mol^{-1}. Interestingly, in the presence of explicit water molecules, the energetic expense for both C–C coupling through **TS1@S$_{WA}$** and the proton-wire step through **TS2@S$_{WA}$** is reduced by ~1 and 15 kcal mol^{-1},

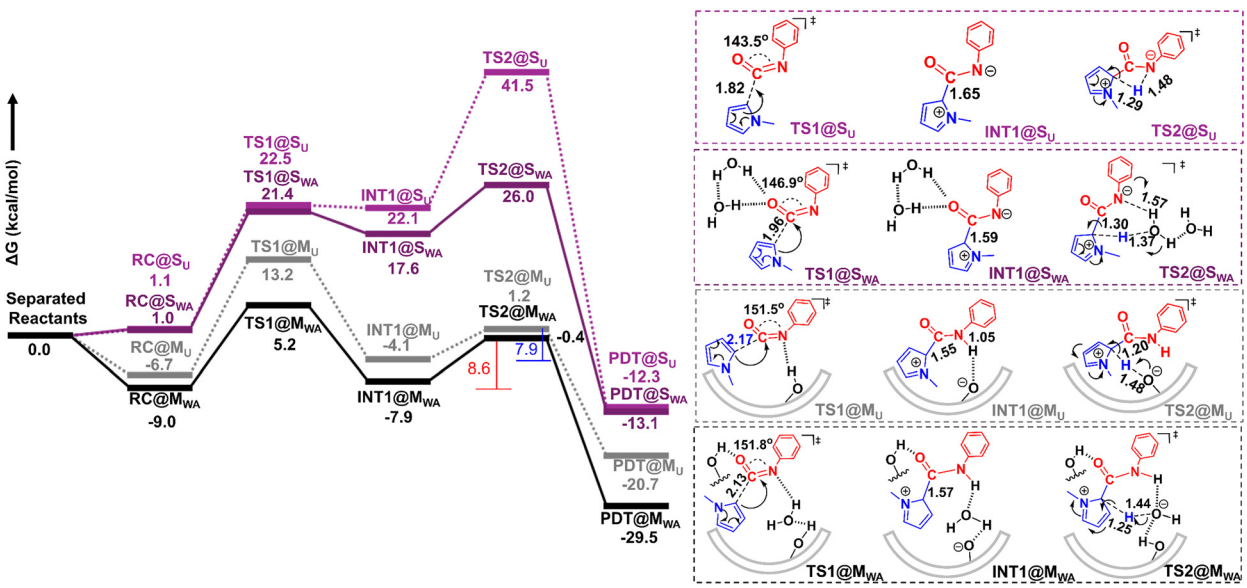

Fig. 1 Gibbs free energy profiles in kcal mol^{-1} at B3LYP-D3BJ/Def2-TZVP/CPCM(CHCl$_3$: H$_2$O = 1 : 1) on the M06-2X/CPCM(CHCl$_3$)/6-31G(d,p)-optimized geometries for the coupling of **2a** and **3a** to yield **4aa** in implicit solvent (S) and assisted by a resorcin-arene monomer (M). @M$_{WA}$ = water-assisted monomer; @M$_U$ = unassisted monomer; @S$_{WA}$ = water-assisted implicit solvent; @S$_U$ = unassisted implicit solvent. Distances shown are in the units of Å.

respectively, indicating the benefit of accommodating water molecules in the vicinity.[20a] Importantly, it was reported by La Manna *et al.* that the reactions of pyrroles and isocyanates under the standard conditions, but in the absence of the capsule, did not lead to completion even after prolonged reaction time (40 hours).[7b] The computed reaction barriers agree to the observation by La Manna and others. In fact, conversion of the rate-determining barrier of **TS2@S$_{WA}$** ($\Delta G^{\ddagger}$ = 26.0 kcal mol^{-1}) to an Eyring rate-constant (k) of 5.4 × 10^{-7} s^{-1} and a half-life of 14.8 days, further intensifying the need for encapsulation.

Next, we consider the assistance of a single monomeric resorcin-arene unit to facilitate the coupling. However, here, the optimum anchorage of the monomer to the substrates through dispersion interactions enables the reactant complexes as the thermodynamic reference to be used to compute the activation-free energy barrier (see Fig. 1). Interestingly, the rearrangement of the two reactants into the intermediate is a mildly endergonic process in the presence (**INT1@M$_{WA}$**, ΔG = 1.1 kcal mol^{-1}) or absence (**INT1@M$_{U}$**, ΔG = 2.6 kcal mol^{-1}) of water assistance with the monomer (**M**) and features a new amido-NH bond. Furthermore, strong, attractive H-bonds stabilize the preceding (**TS1@M$_{WA}$** and **TS1@M$_{U}$**) and succeeding (**TS2@M$_{WA}$** and **TS2@M$_{U}$**) transition states as compared to the significantly energy-intensive reaction in solution (Fig. 1). In fact, encapsulation of the substrates in the single resorcin-arene moiety is impacted by a change in the rate-determining barrier to the initial nucleophilic addition of pyrrole to isocyanate (**TS1@M$_{WA}$** = 14.2 kcal mol^{-1}).

At this stage, our analysis reveals that a large geometric distortion is required to constrain the pyrrole and isocyanate in **TS1**, particularly the angular bending of the N–C–O moiety (Fig. 1, inset). Notably, bifurcation of the activation energy ($\Delta E^{\ddagger}$) into distortion energy (ΔE_{dist}), due to geometric rearrangement, and interaction energy (ΔE_{int}), due to overlapping orbitals of the two substrates, provides meaningful insights into the C–C coupling transition states (Fig. 2).[23] As shown in Fig. 2, ΔE_{dist} dictates the extent of $\Delta E^{\ddagger}$. A detailed investigation shows that **TS1@S$_{U}$** suffers the greatest geometric distortion in the substrates (46.2 kcal mol^{-1}), while **TS1@M$_{WA}$** experiences the least (25.3 kcal mol^{-1}). This observation is in line with the trend in second-order perturbation analyses, $E^{(2)}$, between the donor and the acceptor orbitals[24] in transition states as follows: **TS1@S$_{U}$** (29.0 kcal mol^{-1}) > **TS1@S$_{WA}$** (37.1 kcal mol^{-1}) > **TS1@M$_{U}$** (71.3 kcal mol^{-1}) > **TS1@M$_{WA}$** (97.9 kcal mol^{-1}) (Fig. S1), emphasizing the crucial role of anchorage through non-covalent interactions.

To further understand the factors responsible for the unusual C–C coupling in bulk implicit solvent as compared to monomeric confinement, we analysed the various physical interactions between the substrates and the resorcin-arene monomer using the DLPNO-CCSD(T)/LED methodology. As observed in Table 1, for all the transition states, a large amount of energy is invested in geometric preparation. As expected, detailed investigation demonstrates that $\Delta E^{\ddagger}_{geo\text{-}prep\text{-}3a}$ for substrate **3a** (isocyanate) is the largest in **TS1@S$_{U}$**, followed by **TS1@S$_{WA}$**, **TS1@M$_{WA}$**, and **TS1@M$_{U}$**, arising from the addition of pyrrole to the bent, congested orientation of isocyanate. Hence, a comparison of **TS1@S$_{U}$** and **TS1@S$_{WA}$** shows that the former is hugely destabilizing. Decomposition of $\Delta E^{\ddagger}_{int}$ into dispersive and nondispersive components reveals that London dispersion forces preferentially stabilize the transition states, further emphasizing the crucial role of H-bonding networks.[21c] The attractive dispersion forces are significantly larger in **TS1@M$_{WA}$** compared to its competing transition state, **TS1@M$_{U}$**, reversing the trend of $\Delta E^{\ddagger}_{geo\text{-}prep\text{-}3a}$, and suggesting that a balance of repulsive steric interactions and dispersive interactions is responsible for the desired outcome (Table 1).

Thereby, we diverge on the reactivity inside the capsules, which are inherently reaction vessels, bio-mimicking the active site of several (metallo)enzymes.[25] Notably, for reactions within the confined environment, the self-assembly binding enthalpy is expected to overshadow the entropic cost; hence, reactant complexes would be the reference point necessary to channelize the reaction. Analogous to **RC@C$_{U}$** (Fig. 3), in the experimental study, the authors propose the formation of a heterocomplex **2a** + **3a@C**, on the basis of reactivity inhibition in the presence of competitive hosts such as [NEt$_3$]$^+$ and during H-bond disruption by DMSO.[7b] The optimized geometries of **RC@C$_{U}$** and **RC@C$_{WA}$** show the guest molecules align in a

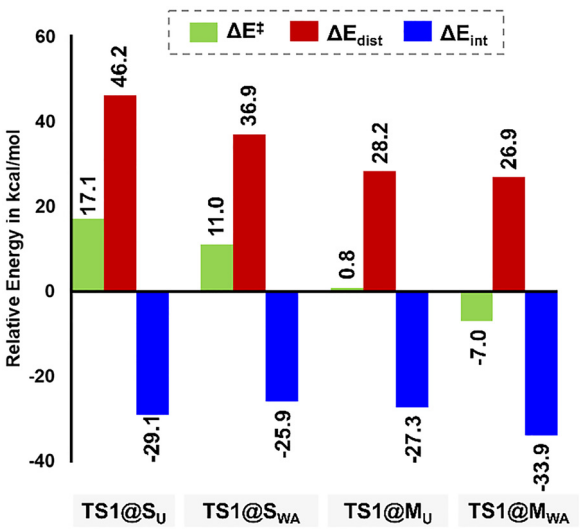

Fig. 2 Energy decomposition analysis **TS1@S$_{U}$**, **TS1@S$_{WA}$**, **TS1@M$_{U}$**, and **TS1@MWA** at B3LYP-D3BJ/Def2-TZVP/CPCM in kcal mol^{-1}.

Table 1 Decomposition of the reaction barriers ($\Delta G^{\ddagger}$) in kcal mol^{-1} calculated by the DLPNO-CCSD(T)/Def2-TZVPP/LED scheme for the C–C coupling in **TS1@S$_{U}$**, **TS1@S$_{WA}$**, **TS1@M$_{U}$**, and **TS1@M$_{WA}$**

	TS1@S$_U$	TS1@S$_{WA}$	TS1@M$_U$	TS1@M$_{WA}$
$\Delta G^{\ddagger}$	41.6	25.6	23.1	18.2
$\Delta E^{\ddagger}$	38.9	23.4	23.0	15.0
$\Delta E^{\ddagger}_{geo\text{-}prep}$	45.7	33.0	25.4	23.7
$\Delta E^{\ddagger}_{geo\text{-}prep\text{-}3a}$	35.0	27.2	18.8	21.4
$\Delta E^{\ddagger}_{int}$	−6.8	−9.6	−2.4	−8.8
$\Delta E^{\ddagger}_{disp}$	−8.4	−7.8	−0.1	−7.5
$\Delta E^{\ddagger}_{no\text{-}disp}$	1.6	−1.8	−2.2	−1.2

T-shape, such that any susceptible steric repulsions within the cavitand are judiciously avoided. The energy barriers for the C–C coupling step in the presence (*via* **TS1@C$_{WA}$**, $\Delta G^{\ddagger}$ = 14.2 kcal mol^{-1}) or absence (*via* **TS1@C$_{U}$**, $\Delta G^{\ddagger}$ = 18.3 kcal mol^{-1}) of the non-structural water molecule inside the capsule are comparable to the reactions with **M**, highlighting similar dispersion effects imposed by the cavity. It may be presumed that intermediate **INT1@M$_{WA}$** is formed through monomer assistance,[14c] and is trapped inside the capsule, facilitated by the capsule's acidity, where it undergoes the proton-wire mechanism (Fig. 3). Indeed, our calculations reveal an enhancement in the average pK_a values of the alcoholic –OH groups on going from **M$_{U}$**(8.2) and **M$_{WA}$**(8.0) to **C$_{U}$**(3.2) and **C$_{WA}$**(2.3). Thus, while **TS2@M$_{WA}$** and **TS2@M$_{U}$** display activation energies in the order of 7.9–8.6 kcal mol^{-1}, the corresponding barriers for **TS2@C$_{WA}$** and **TS2@C$_{U}$** are significantly curtailed to 2.6 and 5.6 kcal mol^{-1}, respectively. Notably, the formation of product **4aa@C$_{WA}$** is calculated to be highly exergonic compared to all the other cases studied.

Furthermore, molecular electrostatic potential (MEP) plots of the catalytic frameworks in **INT1** show an electropositive environment around the –OH groups at the rim, while a distinct electronegative cloud emerges surrounding the phenoxide (O–) moiety (Fig. 4). Additionally, the calculated high nucleophilicity (ω^{-} = −7.8 eV) on the catalytic framework in **INT1@C$_{WA}$** can be directly correlated to the capsule's augmented Brønsted acidity in the presence of the additional hydrogen-bonded water molecule. In fact, the electrophilicity (ω^{+} = 15.1 eV, Table S4) of the pyrrolic C–H unit and the low Wiberg bond index (0.75, Fig. S3) in **INT1@C$_{WA}$** highlight that an electronic balance is achieved in **TS2@C$_{WA}$** for the synchronous C–H activation coupled to the proton shuttle. Thus, our results validate that the water-assisted capsule is the active catalyst. Reduced density gradient (RDG) plots further support our understanding of augmented NCIs in water-assisted transition states for C–C coupling (Fig. S5).

Nevertheless, our work also hints towards the advantage of the ubiquitous presence of water-enriched local domains, which regulate reaction kinetics, selectivity, and mass transfer in natural processes, primarily due to the unique properties of water molecules, such as remote bond polarization, proton shuttling, and the ability to act as co-catalysts.[26] Interestingly, such a natural phenomenon is laterally existent in several industrial-grade processes, working in confined or unconfined environments.[26] Recently, the promotional role of water as an active mediator in C–C coupling reactions has been verified by isotope effect experiments and molecular dynamics simulations.[26b] Indeed, a comparison with one-, two- and three-water molecule-assisted pathways in confinement of the capsule together with an unassisted mechanism strongly support our argument that non-structural water molecules form a bridge between the catalyst and the substrates, polarizing the neighbouring terminals, discharging the steric constrains associated with the optimally oriented substrates, and thereby promoting the C–C coupling step with predominantly low-barriers ranging between 12.7 and 16.4 kcal mol^{-1} as opposed to the unassisted mechanism with a 26.6 kcal mol^{-1} reaction barrier predicted by B3LYP-D3BJ/Def2-TZVP/ALPB(CHCl$_3$)

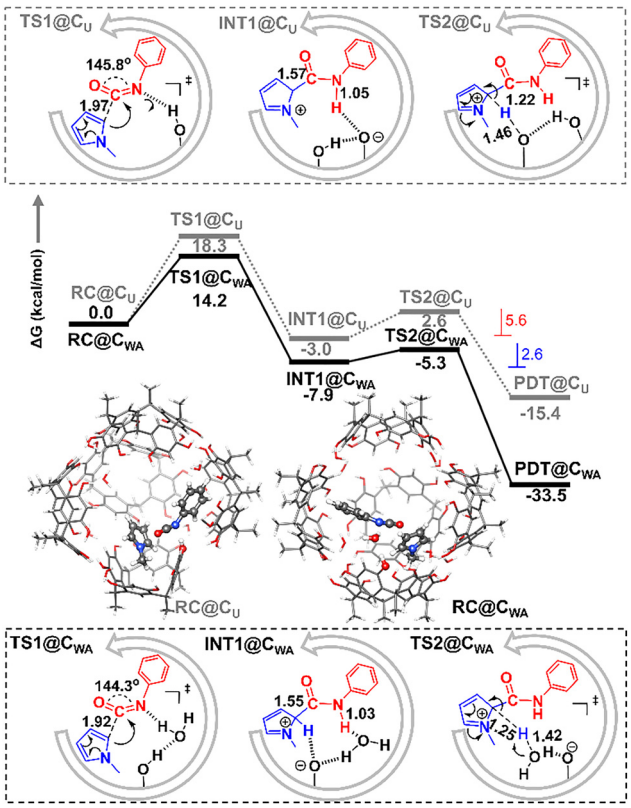

Fig. 3 Gibbs free energy profiles in kcal mol^{-1} at B3LYP-D3BJ/Def2-TZVP/CPCM(CHCl$_3$: H$_2$O = 1 : 1) on ONIOM[M06-2X/CPCM(CHCl$_3$)/6-31G(d,p):PM6]-optimized geometries for the coupling of **2a** and **3a** to yield **4aa** inside capsule **C**. @C$_{WA}$ = water-assisted capsule; @C$_U$ = unassisted capsule. Optimized geometries of **RC@C$_U$** and **RC@C$_{WA}$** (one **M** is omitted for clarity). Colour code: C (grey), O (red), H (white), N (blue).

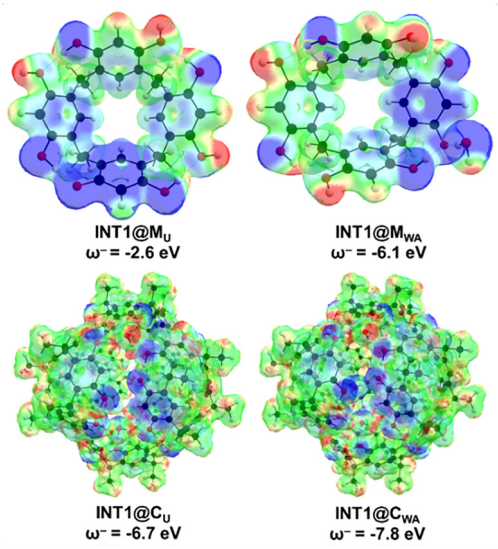

Fig. 4 MEP plot and computed nucleophilicity of the catalytic framework in **INT1**. The colour spectrum ranges from negative (blue) to positive (red) potential within ±0.01 au.

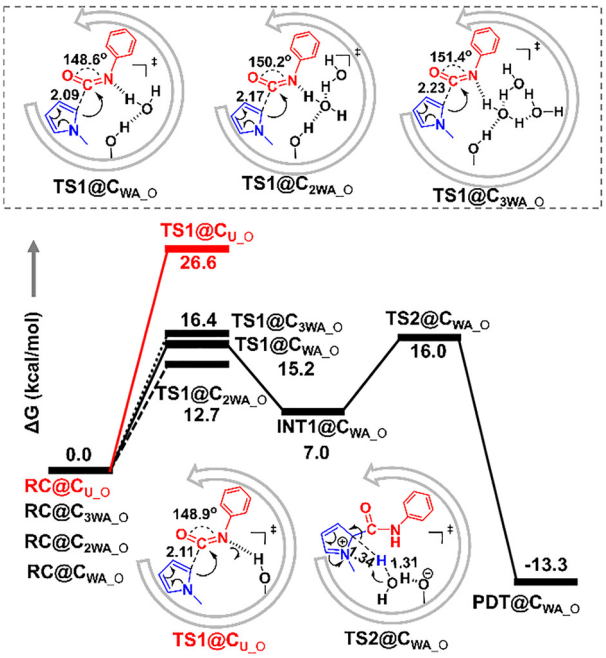

Fig. 5 Gibbs free-energy profiles in kcal mol^{-1} at B3LYP-D3BJ/Def2-TZVP/ALPB($CHCl_3$) on ONIOM[B3LYP-D3(BJ)/ALPB($CHCl_3$)/def2-SVP:XTB][15b] optimized geometries for the coupling of **2a** and **3a** to yield **4aa** inside capsule **C**. @C_{WA} = water-assisted capsule (solid black line); @C_{2WA} = two-water-assisted capsule (dashed black line); @C_{3WA} = three-water-assisted capsule (dotted black line) @C_U = unassisted capsule (shown by red line). Subscript O refers to reactions studied with ORCA 5.0.3.

calculations on ONIOM[B3LYP-D3(BJ)/ALPB($CHCl_3$)/def2-SVP:XTB] optimized geometries (Fig. 5).

Conclusions

In conclusion, we unravelled an unprecedented water-assisted reaction avenue for the coupling of pyrroles and isocyanates to yield amidopyrroles inside a hexameric resorcin-arene capsule. Our results underscore the role of encapsulation together with assistance from non-structurally incorporated water molecules to expedite C–C coupling through nucleophilic addition and synchronous C–H activation and a proton-shuttle mechanism in the self-assembled capsule, as compared to the bulk solvent. Our results strongly suggest the role of a water-rich local domain in providing a balanced hydrophilic encapsulation within a hydrophobic suprastructure, thereby providing the desired stabilization of the micro-solvated transition states. We envisage that our present work will provide new directions towards nanoconfinement-driven chemistry, to achieve high-efficiency and selectivity of organic transformations in hydrophilic encapsulations[27] and diversify the role of water as a co-solvent.

Author contributions

SKM, BG and LR performed all the calculations. LR wrote the manuscript and made the graphics and figures. All the authors gave consent for the final form of the manuscript.

Conflicts of interest

There are no conflicts to declare.

Data availability

The data supporting this article have been included as part of the supplementary information (SI). Supplementary information: Fig. S1–S3 and Tables S1–S4, *XYZ* coordinates and additional computational details. See DOI: https://doi.org/10.1039/d5cp01713k.

Acknowledgements

L.R thanks CSIR, India (01WS(001)/2023-24/EMR-II/ASPIRE), ANRF, India (ANRF/ARG/2025/007177/CS), and SRIC, IIT Kharagpur (IIT/SRIC/FSRG/2025/06) for funding. SKM thanks ICT-IOCB, and BG thanks CSIR-ASPIRE for the research fellowship. This study used the resources of the ParamShakti supercomputing facility of IIT Kharagpur, established under the National Supercomputing Mission of the Government of India and supported by CDAC, Pune.

Notes and references

1 (*a*) D. M. Vriezema, M. C. Aragonès, J. A. A. W. Elemans, J. J. L. M. Cornelissen, A. E. Rowan and R. J. M. Nolte, *Chem. Rev.*, 2005, **105**, 1445; (*b*) M. Mastalerz, *Angew. Chem., Int. Ed.*, 2010, **49**, 5042; (*c*) W. Wang, Y.-X. Wang and H.-B. Yang, *Chem. Soc. Rev.*, 2016, **45**, 2656.

2 (*a*) B. Tang, J. Zhao, J.-F. Xu and X. Zhang, *Chem. – Eur. J.*, 2020, **26**, 15446; (*b*) Q. Zhang, L. Catti and K. Tiefenbacher, *Acc. Chem. Res.*, 2018, **51**, 2107.

3 M. Zhao, H.-B. Wang, L.-N. Ji and Z.-W. Mao, *Chem. Soc. Rev.*, 2013, **42**, 8360.

4 H. Daver, J. N. Harvey, J. Rebek Jr and F. Himo, *J. Am. Chem. Soc.*, 2017, **139**, 15494.

5 L. Catti, Q. Zhang and K. Tiefenbacher, *Chem. – Eur. J.*, 2016, **22**, 9060.

6 (*a*) S. L. Craig, S. Lin, J. Chen and J. Rebek, *J. Am. Chem. Soc.*, 2002, **124**, 8780; (*b*) T. Heinz, D. M. Rudkevich and J. Rebek Jr, *Nature*, 1998, **394**, 764.

7 (*a*) P. La Manna, M. De Rosa, C. Talotta, A. Rescifina, G. Floresta, A. Soriente, C. Gaeta and P. Neri, *Angew. Chem., Int. Ed.*, 2020, **59**, 811; (*b*) P. La Manna, C. Talotta, M. De Rosa, A. Soriente, C. Gaeta and P. Neri, *Org. Lett.*, 2020, **22**, 2590; (*c*) P. La Manna, C. Talotta, G. Floresta, M. De Rosa, A. Soriente, A. Rescifina, C. Gaeta and P. Neri, *Angew. Chem., Int. Ed.*, 2018, **57**, 5423; (*d*) C. Gaeta, C. Talotta, M. De Rosa, P. La Manna, A. Soriente and P. Neri, *Chem. – Eur. J.*, 2019, **25**, 4899.

8 (*a*) R. Silvestri, G. La Regina, G. De Martino, M. Artico, O. Befani, M. Palumbo, E. Agostinelli and P. Turini, *J. Med. Chem.*, 2003, **46**, 917; (*b*) G. Montà-González, D. Bastante-Rodríguez, A. García-Fernández, P. Lusby, R. Martínez-Máñez and V. Martí-Centelles, *Chem. Sci.*, 2024, **15**, 10010.

9 L. R. MacGillivray and J. L. Atwood, *Nature*, 1997, **389**, 469.
10 D. A. Poole III, S. Mathew and J. N. H. Reek, *J. Am. Chem. Soc.*, 2021, **143**, 16419.
11 A. Katiyar, J. C. F. Sovierzoski, P. B. Calio, A. A. Vartia and W. H. Thompson, *Chem. Commun.*, 2019, **55**, 6591.
12 L. Avram and Y. Cohen, *J. Am. Chem. Soc.*, 2002, **124**, 15148.
13 F. Sebastiania, T. A. Bender, S. Pezzottia, W.-L. Li, G. Schwaab, R. G. Bergman, K. N. Raymond, F. Dean Toste, T. Head-Gordon and M. Havenith, *Proc. Natl. Acad. Sci. U. S. A.*, 2020, **117**, 32954.
14 (*a*) V. Vaissier Welborn, W.-L. Li and T. Head-Gordon, *Nat. Commun.*, 2020, **11**, 415; (*b*) H. Daver, J. Rebek Jr and F. Himo, *Chem. – Eur. J.*, 2020, **26**, 10861; (*c*) P. La Manna, C. Talotta, C. Gaeta, Y. Cohen, S. Slovak, A. Rescifina, P. Della Sala, M. De Rosa, A. Soriente and P. Neri, *Org. Chem. Front.*, 2022, **9**, 2453.
15 (*a*) M. J. Frisch, G. W. Trucks, H. B. Schlegel, G. E. Scuseria, M. A. Robb, J. R. Cheeseman, G. Scalmani, V. Barone, B. Mennucci, G. A. Petersson, *et al.*, *Gaussian 09 (Revision A.02)*, Gaussian, Inc., Wallingford CT, 2009; (*b*) F. Neese, *Wiley Interdiscip. Rev. Comput. Mol. Sci.*, 2022, **12**, e1606.
16 L. W. Chung, W. M. C. Sameera, R. Ramozzi, A. J. Page, M. Hatanaka, G. P. Petrova, T. V. Harris, X. Li, Z. Ke, F. Liu, H.-B. Li, L. Ding and K. Morokuma, *Chem. Rev.*, 2015, **115**, 5678.
17 (*a*) A. D. Becke, *J. Chem. Phys.*, 1993, **98**, 5648; (*b*) Y. Zhao and D. G. Truhlar, *Theor. Chem. Acc.*, 2008, **120**, 215.
18 (*a*) S. Grimme, J. Antony, S. Ehrlich and H. A. Krieg, *J. Chem. Phys.*, 2010, **132**, 154104; (*b*) S. Grimme, S. Ehrlich and L. Goerigk, *J. Comput. Chem.*, 2011, **32**, 1456.
19 X. Zhang and R. S. Paton, *Chem. Sci.*, 2020, **11**, 9309.
20 (*a*) P. L. da Silva, L. Guimaraes and J. R. Pliego Jr, *J. Phys. Chem. B*, 2013, **117**, 6487; (*b*) M. Bursch, J.-M. Mewes, A. Hansen and S. Grimme, *Angew. Chem.*, 2022, **134**, e202205735; (*c*) A. K. Singh and L. Roy, *Eur. J. Inorg. Chem.*, 2023, e202300412.
21 (*a*) D. Yepes, F. Neese, B. List and G. Bistoni, *J. Am. Chem. Soc.*, 2020, **142**, 3613; (*b*) G. Bistoni, A. Altun, Z. Wang and F. Neese, *Acc. Chem. Res.*, 2024, **57**, 1411; (*c*) S. K. Mahapatra, B. Ghosh and L. Roy, *ChemCatChem*, 2025, **17**, e01069.
22 (*a*) R. G. Parr, L. Von Szentpaly and S. B. Liu, *J. Am. Chem. Soc.*, 1999, **121**, 1922; (*b*) J. L. Gazquez, A. Cedillo and A. Vela, *J. Phys. Chem. A*, 2007, **111**, 1966.
23 (*a*) M. Baidya, D. Maiti, L. Roy and S. De Sarkar, *Angew. Chem., Int. Ed.*, 2022, **61**, e202111679; (*b*) L. Roy, B. Ghosh and A. Paul, *J. Phys. Chem. A*, 2017, **121**, 5204–5216; (*c*) W. J. van Zeist and F. M. Bickelhaupt, *Org. Biomol. Chem.*, 2010, **8**, 3118–3127; (*d*) R. Khuntia, S. K. Mahapatra, L. Roy and S. C. Pan, *Chem. Sci.*, 2023, **14**, 10768.
24 A. K. Singh and L. Roy, *Chem. Phys. Chem.*, 2024, **25**, e202400533.
25 (*a*) H. S. Ali and S. P. de Visser, *Chem. – Eur. J.*, 2022, **28**, e202104167; (*b*) R. N. Manna, T. Malakar, B. Jana and A. Paul, *ACS Catal.*, 2018, **8**, 10043; (*c*) L. Roy, *ChemCatChem*, 2018, **10**, 3683.
26 (*a*) G. Li, B. Wang and D. E. Resasco, *ACS Catal.*, 2020, **10**, 1294 and references therein; (*b*) D. T. Ngo, Q. Tan, B. Wang and D. E. Resasco, *ACS Catal.*, 2019, **9**, 2831–2841.
27 Shashi, S. Das, A. Datta and J. Dasgupta, *J. Phys. Chem. Lett.*, 2025, **16**, 11464–11471.

